Environmental Research 228 (2023) 115757

Contents lists available at ScienceDirect

Environmental Research

journal homepage: www.elsevier.com/locate/envres

Highly graphitic Fe-doped carbon xerogels as dual-functional electro-Fenton catalysts for the degradation of tetracycline in wastewater

A. Barranco-López, A.I. Moral-Rodríguez, E. Fajardo-Puerto, A. Elmouwahidi, E. Bailón-García *

Carbon Materials Research Group, Department of Inorganic Chemistry, Faculty of Sciences, University of Granada, Campus Fuentenueva s/n, 18071, Granada, Spain

ARTICLE INFO

Handling Editor: Aijie Wang

Keywords:
Oxygen reduction reaction
Carbon xerogels
Fe-doping
Graphitization
Hydrogen peroxide
Electro-fenton

ABSTRACT

Fe-doped carbon xerogels with a highly developed graphitic structure were synthesized by a one-step sol-gel polymerization. These highly graphitic Fe-doped carbons are presented as promising dual-functional electro-Fenton catalysts to perform both the electro-reduction of O_2 to H_2O_2 and H_2O_2 catalytic decomposition (Fenton) for wastewater decontamination. The amount of Fe is key to the development of this electrode material, since affects the textural properties; catalyzes the development of graphitic clusters improving the electrode conductivity; and influences the O_2-catalyst interaction controlling the H_2O_2 selectivity but, at the same time is the catalyst for the decomposition of the electrogenerated H_2O_2 to $OH^{\bullet}$ radicals for the organic pollutants oxidation. All materials achieve the development of ORR via the 2-electron route. The presence of Fe considerably improves the electro-catalytic activity. However, a mechanism change seems to occur at around −0.5 V in highly Fe-doped samples. At potential lower than −0.5 eV, the present of $Fe^{\delta+}$ species or even Fe–O–C active sites favour the selectivity to 2e-pathway, however at higher potentials, $Fe^{\delta+}$ species are reduced favoring a O–O strong interaction enhancing the 4e-pathway. The Electro-Fenton degradation of tetracycline was analyzed. The TTC degradation is almost complete (95.13%) after 7 h of reaction without using any external Fenton-catalysts.

1. Introduction

New and more stable pollutants are being increasingly detected in surface and groundwater due to the population growth and the increase of its living standard (Giordano et al., 2019; Kumar and Ladha, 2011; Yadvinder-Singh et al., 2014). Among these emerging pollutants, pharmaceutical compounds are of greatest concern due to, in most cases, are not regulated and cannot be removed by traditional wastewater treatment methods being discharged into the environment. Consequently, these pollutants accumulate in the different water resources being a potential risk to the environment and health (Mailler et al., 2016; Rosal et al., 2010). Therefore, efficient management processes are required to ensure the environment protection and the availability of present and future water resources.

Advanced oxidation processes (AOPs) are powerful water treatment technologies in which the high oxidation power of hydroxyl radicals (OH·) is used for the effective removal of organic pollutants (Belgiorno et al., 2007; Lata et al., 2015; Sannino, 2020). These radicals can be *in situ* generated by different methods: ozone/hydrogen peroxide combination, Fenton and photo-Fenton processes, heterogeneous photocatalysis, among others, and can oxidize persistent organic compounds, enabling their complete mineralization to CO_2, H_2O and other stable inorganic compounds (Oturan and Aaron, 2014).

Among AOPs, the Fenton technology is very attractive due to its simplicity, low cost, high yield and the low toxicity of the Fenton reagent (a mixture of Fe^{2+} and H_2O_2) (Zhang et al., 2019). Although the Fenton rection mechanism remains uncertain because the identity of the main species involved is unclear, basically, the traditional Fenton reaction consists in the addition of H_2O_2 in presence of iron salts in an acidic medium, for the generation of OH· radicals (Equation (1)) (Litter and Slodowicz, 2017). The resulting ferric ions (Fe^{3+}) can also react with H_2O_2, leading to regeneration of Fe^{2+} species (Eq. (2)). However, the reactivity of Fe^{3+} with H_2O_2 is much lower than that of Fe^{2+}, and this is considered to be the limiting reaction of the process (Ameta et al., 2018). In addition to the formation of hydroxyl radicals (OH·), perhydroxyl radicals (HO_2·) are also generated, however, these radicals are less oxidizing than $OH^{\bullet}$.

$$Fe^{2+} + H_2O_2 \rightarrow Fe^{3+} + OH^- + OH^{\bullet} \quad (1)$$

$$Fe^{3+} + H_2O_2 \rightarrow Fe^{2+} + HO_2^{\cdot} + H^+ \quad (2)$$

* Corresponding author.
E-mail address: estherbg@ugr.es (E. Bailón-García).

https://doi.org/10.1016/j.envres.2023.115757
Received 31 January 2023; Received in revised form 6 March 2023; Accepted 22 March 2023
Available online 25 March 2023
0013-9351/© 2023 The Authors. Published by Elsevier Inc. This is an open access article under the CC BY-NC-ND license (http://creativecommons.org/licenses/by-nc-nd/4.0/).

Organic pollutants + $OH^{\bullet} \rightarrow$ *Degradation products* (3)

In addition to Fe^{2+}, other metallic ions such as Cu^{+}, Co^{2+} or Mn^{2+} can also promote similar redox reactions, known as Fenton-type catalysts (Ameta et al., 2018; Matyszczak et al., 2020).

The Fenton process takes place under normal pressure and temperature conditions and the reagents are easily available. However, the Fe^{2+} consumption (eq. (1)) is faster than its regeneration (Eq. (2)). Thus, a sludge is formed during the process due to the precipitation of a large amount of ferric hydroxide, which poses additional separation and removal problems, especially when treating large volumes of water. In addition, Fe^{2+} concentrations as high as 40–80 ppm are required which is a major drawback of homogeneous Fenton processes. In an attempt to avoid these sludge generation problems, Fenton active phase is often supported on porous materials such as carbon (Navalon et al., 2011). However, although the Fe^{2+} leaching is reduced, it is still present. Therefore, the precipitation of iron oxides as a solid sludge, the narrow margin of working pH and the risks and costs of handling, transporting, and storing highly concentrated H_2O_2 represent the major shortcomings of this treatment.

In this respect, the Electro-Fenton (EF) process, a new development of the Fenton process, has aroused great interest (Brillas et al., 2009). In the EF, H_2O_2 is produced *in situ* by the reduction of O_2 in the cathode. On the other hand, the regeneration of Fe^{2+}, which is necessary for the course of the reaction, is more effective since, in addition to being produced by different reduction processes involving H_2O_2 or organic radical intermediates, it can also be produced through direct reduction at the cathode. Therefore, the main advantages of electro-Fenton process are the on-site generation of H_2O_2 which evade the costs and risks associated with its handling, storage and transport; the possibility to control the kinetics of oxidative degradation and to perform studies on the reaction mechanisms; higher rate of contaminant removal due to the catalytic activity of the Fenton reagent through continuous regeneration of Fe^{2+} avoiding the additional use of reagents and sludge formation; and the potential to achieve total mineralization at relatively low cost by optimising the operating parameters (Brillas et al., 2009; Oturan and Aaron, 2014).

Since H_2O_2 is generated *in situ* by the reduction of O_2, the study of the oxygen reduction reaction (ORR) is of particular importance for the EF process. ORR can occur via two routes: 4e- or 2e-generating H_2O or H_2O_2, respectively. Therefore, to ensure and optimise the EF process, materials that catalyze ORR via the 2e-route and maximize peroxide production must be designed. The active sites/oxygen species binding strength is the critical factor controlling activity and selectivity in ORR (Jiang et al., 2019a). The key for ORR to proceed through the two-electron pathway is to preserve the O–O bond avoiding its dissociation, so a not too strong but sufficient interaction to overcome the reaction barrier is required to obtain H_2O_2 (Kulkarni et al., 2018a) since a very strong active site-oxygen species interaction results in dissociation of O_2 and, consequently, favours the selectivity towards H_2O. This active site-oxygen species interaction, and hence the ORRperformance, depends on the catalyst properties such as the metal presence and its nature and dispersion; the graphitization degree or conductivity of carbonaceous support; and the catalysts textural properties. Many noble metal alloys, such as Pd–Au, Pt–Hg, Pt–Ag, Ag–Hg and Pd–Hg possess considerably high catalytic activity for the production of H_2O_2 (Chang et al., 2020; Zhao et al., 2018). However, the prohibitive cost and the scarcity of noble metals make these catalysts not industrially viable and, therefore, new alternatives based on non-noble metals are being sought. In this respect, carbon materials are presented as a promising candidate as ORR electrocatalysts since they are produced at low cost from an wide variety of abundant carbonaceous precursors. Carbon materials, such as graphite, activated carbons, carbon felt, carbon nanotubes, activated carbon fibres, cross-linked glassy carbon, carbon sponges and carbon gas diffusers have exhibit apparent advantages for the production of H_2O_2 because of their high specific surface area, tuneable surface chemistry and high electrical conductivity and, therefore, were used as effective cathodes electrodes for the EF (Divyapriya and Nidheesh, 2020; Oller et al., 2021). Among the carbonaceous materials described in the literature for EF, graphene stands out for its excellent conductivity and high mechanical strength. Chen-Yu Chen et al. (2016) synthesized thermally reduced graphene with a high specific surface area (308.8 $m^2\ g^{-1}$) and a large oxygen content (10.3% at) and shown that this acts as excellent catalyst for the development of ORR via two-electron pathway with high reactivity. Furthermore, it has been shown that the introduction of defects in carbon-based electrocatalysts enhances the selectivity to the two-electron pathway and thus, achieves efficient H_2O_2 generation performance since these defects act as active sites. In this regards, N-doping of the carbon matrix is an effective strategy to enhance the electrocatalytic ORR since appropriately change the mode of adsorption of O_2 and introduce highly efficient active sites (Li and Zhang, 2019). Thus, the tunning of the chemical structure of graphene by the introduction of oxygen or nitrogen functionalities significantly improves the selectivity of the ORR. The stable oxygen functional groups of rGO are responsible of the adsorption of dissolved oxygen and its subsequent conversion to H_2O_2 whereas in N-doped graphene the selectivity to ORR via two electrons is ascribed to synergistic effects such as a favourable electronic structure, distribution of N atoms and increased porosity (Divyapriya and Nidheesh, 2020).

Nonetheless, despite the advances in ORR achieved for the *on-site* production of H_2O_2, the EF process still requires the use of two catalysts: one selective to the reduction of oxygen to H_2O_2 and another Fenton-type catalyst for the transformation of H_2O_2 to hydroxyl radicals. Many efforts are being made in recent years to develop materials with dual functionality for the electroreduction of oxygen to H_2O_2 and Fenton. However, the preparation of heterogeneous EF catalysts with high selectivity and activity towards ORR via the two-electron pathway is challenging, since the active sites for Fenton are mainly transition metals that in the main catalyze oxygen reduction via the 4e-pathway (which does not generate H_2O_2). Only few researchers regarding this important challenge were found in bibliography. The main strategies are focused on the use of heteroatoms-doped carbon materials or carbon encapsulated Fenton-type metals/carbon composite that moderate the metal activity and provided active site for H_2O_2 generation by ORR 2e-route presenting metal sites for the activation of *in situ* generated H_2O_2 to ·OH radicals required for the organic pollutant degradation. Li et al. (2022) demonstrated that heteroatom-doped carbon materials are able to convert H_2O_2 to •OH radicals without the needed of a Fenton metal catalyst. For that, the authors synthesized a O, F-codoped carbon bifunctional catalyst by carbonization of polyvinylidene fluoride and proposed that the H_2O_2 generation depend principally of the ratio C–O/C═O (optimal value in 4), while that the activation to •OH occurs on the semi ionic C–F bonds. A similar fact was observed by Yang et al. (2019) using N-doped graphene. They found that the bifunctional effect is attributed to the presence of N-graphite which influence the H_2O_2 generation and N-pyrrolic responsible of H_2O_2 activation. Similarly, Haider et al. (2019) synthetized *in situ* an electrode from polyaniline derived N-doped carbon nanofibers with bifunctional activity in EF which was attributed to the content of C═C, oxygen groups and N-graphitic which enhance the H_2O_2 generation which can further activate by N-pyridinic to generate the •OH radicals. In turn, Qin et al. (2021) used as bifunctional metal-free cathode based on O-doped carbon nanotubes. They attributed the excellent metal free EF behaviour of this catalyst to the defects and the C-sp^3 that enhances the oxygen adsorption promoting the H_2O_2 production and to the –C═O active sites that are associated to the •OH production.

However, to increase the generation of ·OH radicals and thus, enhance the Electro-Fenton degradation, the use of Fenton-type metals are required. In order to modulate the activity of this metal-based materials, metals are encapsuled in core/shell structures of carbon and highly conductive carbon-based materials such as carbon fibers, carbon

black or carbon nanotubes are also introduced. Ghasemi et al. (2020) prepared a cathode with carbon nanotubes (CNTs) and CuFe nano-layered double hydroxide showing that the incorporation of CNTs improve the H_2O_2 generation, and the atoms of Cu and Fe were the responsible of the generation of OH•. Luo et al. (2020) prepared Cu-doped Fe@Fe_2O_3 core-shell nanoparticles loaded on the nickel foam as cathode, and determined that Cu^0 and Fe^0 react with O_2 producing H_2O_2; Fe^{+2}, Cu^+ are responsible of the •OH generation from the in-situ generated H_2O_2. Moreover, they proposed that Fe^{2+} and Cu^{2+} additional EF active sites could be generated from redox process between Cu^+ and Fe^{3+} and replacement reaction between Cu^{2+} and Fe^0. Sun et al. (2022) synthesized a nickel foam cathode co-modified with core-shell CoFe alloy/N-doped carbon (CoFe@NC) and carbon nanotubes (CNTs), where the production of H_2O_2 was attributed to CNTs and the activation to OH• to CoFe@NC through Fe^{2+} and Co^{2+} oxidation to Fe^{3+} and Co^{3+} which are again reduced by Co^0/$Fe^0$and the electric field.

Owing to this overview, it is important to highlight that only few research are found regarding the synthesis of high performance bifunctional catalyst for generation and activation of H_2O_2 in the cathode and most of them imply the encapsulation of metal particles by expensive and tedious methods. So, in this work a facile and direct synthesis of Fe-doped carbon xerogels by sol-gel polymerization of organic monomers was proposed and these materials were tested in the ORR with the aim to analyze the effect of the Fe concentration on the textural and chemical properties of the final carbon material and thus, on its performance and selectivity in ORR with the aim of develop suitable catalysts with dual functionality for the electro-Fenton degradation of emerging pollutants. For that, tetracycline was selected as a typical emerging drug frequently detected in water. Tetracycline is a commonly used antibiotic due to its broad-spectrum antimicrobial activity being bioaccumulation in the environment causing serious heath and ecosystem risks through the creation of antibiotic resistant bacteria and genes (Luo et al., 2020).

2. Experimental

2.1. Synthesis of Fe-doped carbon nanocomposites

Fe-doped carbon xerogels (FeCX-Y) were synthesized with a Fe loading (Y) varying from 0 to 0.8% by sol-gel polymerization of resorcinol and formaldehyde in presence of iron (II) acetate as polymerization catalyst and Fe precursor. Briefly, an aqueous mixture of resorcinol (R) and formaldehyde (F) was prepared with a R/F and R/W molar ratio of 1/2 and 1/13, respectively. The proper amount of iron acetate to obtained Fe contents of 0.2, 0.4 and 0.8% in the final FeCX-Y carbon material was added to this RF solution under stirring until total dissolution. This mixture was transferred to glass tubes of an inner diameter of 5 mm which were sealed and submitted to a thermal program consisting of 1 day at 50 °C and 3 days at 80 °C to obtain the hydrogel. Then, the organic gels were unmolded and placed in acetone for 3 days to favour the subsequent drying and preserve the porosity. Finally, the organic gels were drying using a microwave oven under Ar atmosphere and carbonized at 800 °C for 2 h using a temperature ramp of 2 °C/min.

2.2. Textural and chemical characterization

The textural properties of samples were characterized by N_2 adsorption-desorption at −196 °C. For that, the samples were previously outgassed overnight at 110 °C under high vacuum (10^{-6} mbar). From adsorption data, the specific surface area (S_{BET}) and the micropore volume (W_0) and mean width (L_0) were obtained by applying the BET and the Dubinin-Radushkevich (DR) equations, respectively. The total pore volume ($V_{0.95}$) was obtained as the N_2 adsorption volume at 0.95 relative pressure. Finally, the mesopore volume (V_{MESO}) was calculated as $V_{0.95}$-W_0 (N_2) by applying the Gurvich rule.

The texture and morphology of samples were observed by scanning electron microscopy (SEM) using a FEI microscope model Quanta 400 and the development of graphitic clusters and Fe particle dispersion were studied by high-resolution electron microscopy (HRTEM) in a Thermo Fisher Scientific microscope model Talos F200X.

X-ray diffraction was performed to analyze the crystallinity of Fe-doped carbon materials using a Bruker D8 Venture X-ray diffractometer with Cu Kα radiation. The XRD patterns were recorded in a 2θ range of 5°–75°. The Debye-Scherrer equation was applied to the more intense diffraction peak to calculate the metal average crystal size.

The graphitization degree of the carbon samples was studied by Raman spectroscopy. Raman spectra were obtained using a Micro-Raman JASCO NRS-5100 dispersive spectrophotometer with a 532 nm laser line.

X-ray photoelectron spectroscopy (XPS) was performed in a Kratos Axis Ultra-DLD spectrometer equipped with a hemispherical electron analyzer connected to a detector DLD (delay-line detector) and a Al-Kα monochromator of a power of 600 W. The X-ray source is a Mg/Al double anode of 450 W.

Thermogravimetric analysis (TGA) and inductively coupled plasma optical emission spectrometry (ICP-OES) were performed to analyze the thermal stability of carbon samples and to determine the total metal content using a TGA/DSC1 Thermogravimetric Analyzer from METTLER-TOLEDO and an Optima 8300 ICP-OES from PerkinElmer, respectively.

The Fe leaching from the catalysts in the treated water was analyzed by atomic absorption spectroscopy using an VARIAN SPECTRAA 140 atomic absorption spectrometer.

2.3. Electro-chemical characterization

The Fe-doped carbons were electrochemically characterized in a Biologic VMP Multichannel potentiostat using a Rotating Ring-Disk Electrode (RRDE) (Metrohm AUTOLAB RDE-2, 3 mm Glassy Carbon tip) where the carbon sample was deposited as working electrode, a platinum wire as counter electrode and Ag/AgCl reference electrode. The working electrode was prepared by depositing on the RRDE tip 20 μL of a ink, consisting of 5 mg of sample dispersed in 1 mL of a Nafion solution (1/9 v:v Nafion 5%/water), and dried under infrared radiation.

Cyclic Voltammetry experiments (CV) were performed both in O_2-saturated 0.1 M KOH solution and in a 0.1 M KOH solution completely degassed (by bubbling N_2). The sweeping potential rate was 50 mV/s, from 0.4 V to −0.8 V (vs. Ag/AgCl) while RRDE was rotating at 1000 rpm. To evaluate the catalytic performance and to obtain the onset potential (E_{ONSET}), Linear Sweep Voltammetry experiments (LSV) were measured in an O_2-saturated 0.1 M KOH solution at different rotation rates from 500 rpm to 4000 rpm. The experiments were conducted from 0.4 V to −0.8 V (Ag/AgCl) at a sweep rate of 5 mVs^{-1}.

The number of electrons transferred (n), and the kinetic density current (j_k) were obtained by fitting the LSV disc electrode data to the Koutecky-Levich model. In turn, overall electron transfer number (n) and the percentage of hydrogen peroxide produced (H_2O_2%) were also calculated from the currents of the platinum ring measured during the LSV experiments according to Equations (4) and (5), respectively.

$$n = \frac{4 \cdot I_D}{I_D - \frac{I_R}{N}} \tag{4}$$

$$H_2O_2\% = 100 \cdot \frac{2 \cdot \frac{I_R}{N}}{I_D - \frac{I_R}{N}} \tag{5}$$

where I_R and I_D are the ring and the disk currents, respectively and N is the collection efficiency of the RRDE (N = 0.245).

2.4. Electro-fenton tests

To prepare the Electro-Fenton electrodes, a homogeneous mixture of

the finely ground Fe-doped carbon xerogel and polytetrafluoroethylene (PTFE) binder at a mass ratio of 90:10 was prepared and dried at 80 °C overnight. Then, 50 mg of this mixture was pasted in a graphite paper (50 mm × 8 mm).

Tetracycline (TTC) was selected as emerging pollutant to evaluate the activity of the dual-functional electrocatalysts in the EF tests. Prior to the Electro-Fenton (EF) tests, adsorption kinetics and isotherms were performed using the carbon xerogel/PTFE paste. TTC adsorption kinetic was studied with the aim to obtain the time needed to achieve the adsorption equilibrium at saturation, being 8 h (results not shown). Then, the TTC adsorption isotherms was obtained by using 0.005 g of the carbon xerogel/PTFE mixture and 10 mL of TTC solutions (in 0.5 M Na_2SO_4) at concentrations ranging from 10 to 80 mg L^{-1}. The suspensions were mechanically shaken for 24 h to ensure equilibrium was reached and the equilibrium concentration determined at 358 nm using a UV-spectrophotometer model UV-2600i Shimadzu.

The EF tests were performed in a three electrodes glass cell controlled by a Biologic VMP multichannel potentiostat (BioLogic Science Instruments) using Ag/AgCl as reference electrode and a Pt-wire as the counter electrode. Once known the adsorption capacity of the sample, the initial concentration of the EF test was fixed to obtain a final concentration of 10 mg L^{-1} after the adsorption in dark. For that, 100 mL of TTC solution of the proper concentration in 0.5 M Na_2SO_4 as electrolyte was contacted with the EF electrode and maintain for 24 h in dark and under stirring to saturate the carbon sample. The pH value of electrolyte was adjusted at 7.0 by NaOH. After that, a voltage of −0.6 V (potenciostatic mode) is applied under O_2 bubbling to start the EF experiment. The O_2 gas was bubbled for 30 min before the experiment started in order to saturate the solution and continuously bubbled during the experiment time. Aliquots of 1 mL were taken periodically from the glass cell, and its concentration was immediately analyzed using a UV-spectrophotometer. The total organic carbon (TOC) was determined with a TOC-VCSH Shimadzu equipment to evaluate the mineralization degree.

3. Results and discussion

3.1. Morphological characterization

The samples morphology was studied by SEM. Most representative images of pure and Fe-doped carbon samples are shown in Fig. 1. Note that all samples show a morphological structure characteristics of carbon gels; nanometric primary particles fused forming a coral-type structure leaving porosity between them. It seems that these primary particles are smaller and more fused in the case of Fe-doped CX samples leaving narrower porosity, but the morphology of all Fe-doped samples is very similar despite the different iron content.

In order to analyze the Fe dispersion and the development of graphitic clusters by Fe nanoparticles, HRTEM was performed (Fig. 2). Highly graphitic samples were obtained despite the low amount of Fe in the samples (less than 0.8%). Graphitic clusters are clearly identified in Fe-doped samples while they are not present in undoped CX. Moreover, note that the amount of those graphitic clusters increases by increasing the amount of Fe in the samples (FeCX-0.2 < FeCX-0.4 < FeCX-0.8). This indicates that the presence of Fe catalyzes the development of graphitic clusters so that with a content as low as 0.8% the sample is almost entirely composed of such clusters. This carbon graphitization by iron particles has already been pointed out in previous work (Castelo-Quibén et al., 2018; Maldonado-Hódar et al., 2004, Maldonado-Hódar et al., 2000). These graphitic clusters have a rounded shape but only some of them are surrounding a Fe particle of around 10 nm. This could indicate that the same Fe nanoparticle catalyzes the growth of several graphitic clusters and so, a not very high content of Fe is required for the almost entirely graphitization of the carbon matrix. It is important to remark that these highly graphitic Fe-doped carbon xerogels were obtained at a relatively low carbonization temperature of 800 °C. Usually, the graphitization process of amorphous carbons required the application of high temperatures (>2500 °C) (Zhai et al., 2011). Note also that Fe particles are well dispersed on the carbon matrix, however, the Fe particle size (D_{Fe}) seems to increase by increasing the Fe amount within the carbon matrix.

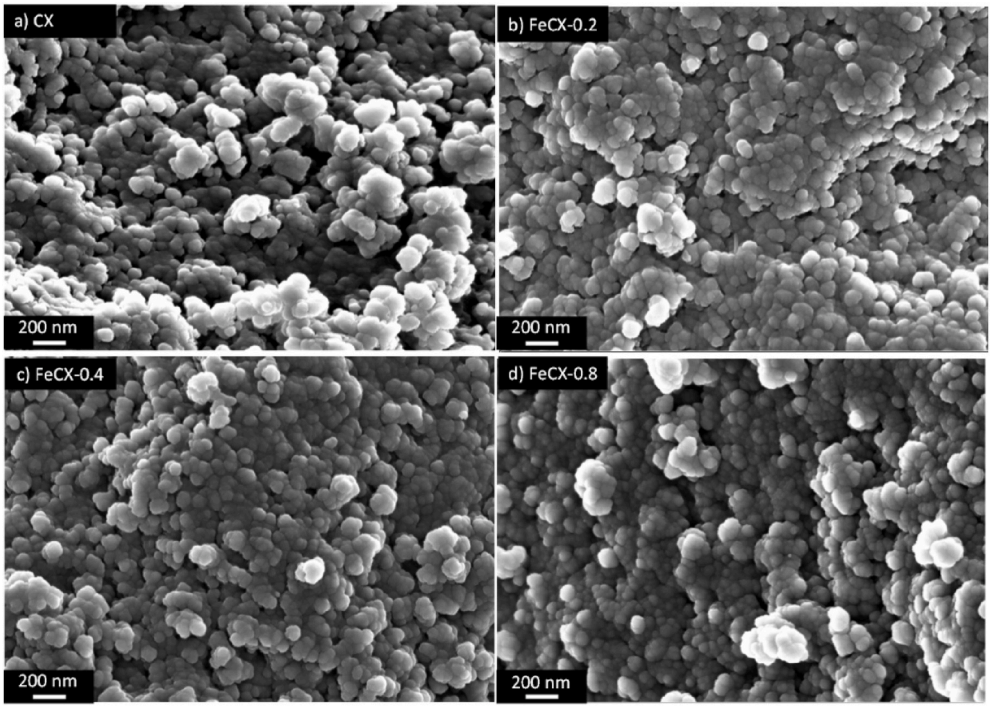

Fig. 1. SEM images of pure (CX) and Fe-doped (FeCX-Y) carbon samples.

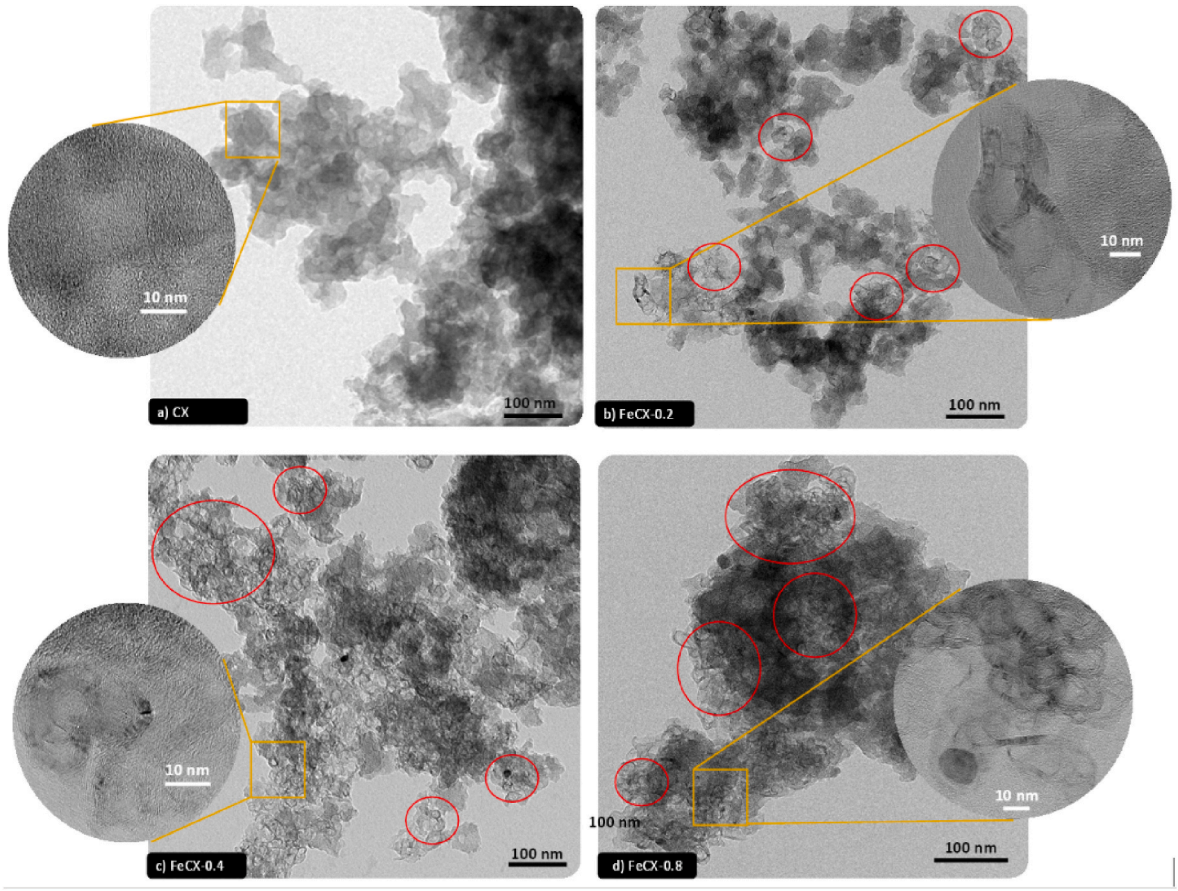

Fig. 2. HRTEM images of pure (CX) and Fe-doped (FeCX-Y) carbon samples.

3.2. Textural characterization

The different morphology and the development of graphitic clusters observed by SEM and HRTEM, respectively, affect the textural properties of samples. The textural properties of pure CX and FeCX-Y samples were analyzed by N_2 and CO_2 adsorption isotherms at −196 and 0 °C, respectively. N_2 adsorption-desorption isotherms are plotted in Fig. 3a and the corresponding results are summarized in Table 1.

CX sample shows a type I-II hybrid isotherm (IUPAC classification) characteristics of micro-macroporous solids in which the high N_2 adsorption at very low relative pressure manifests the existence of micropores and the fast N_2 adsorption increase at relative pressures close to 1 indicates the presence of macropores (Alothman, 2012; Lowell et al., 2004; Sing, 2001). A similar isotherm shape is observed for Fe-doped CX samples but the N_2 uptake at low relative pressures is lower than for CX counterpart, denoting lower microporosity, and a N_2 adsorption is also observed at medium relative pressures manifesting the presence of mesopores. This are in good agreement with the SEM observations. In carbon gels the microporosity is usually ascribed to the intraparticle voids whereas the meso, macroporosity is related with the interparticle voids. In the case of Fe-doped samples, the primary particles are smaller and are more fused than for CX counterpart, thus, leaving narrower interparticle voids (mesopores). This porosity narrowing was also corroborated by analyzing the pores size distribution of samples by QSDFT and BJH methods. The BJH and the DFT pore size distributions (Fig. 3b and **c**, respectively) show that the CX wide porosity ($L > 2$ nm) present a monomodal distribution with a maximum centered at an average diameter of 44.9 nm (near of macroporosity range) with some mesoporosity at 3.6 nm. The Fe-doping produces a decrease in the average diameter to around 30 nm and also an increase in the volume of narrower mesopores (3–10 nm).

The surface area (S_{BET}) and the micro and mesopores volume (W_0 and V_{meso}, respectively) and width (L_0 and L_{meso}, respectively) obtained from the analysis of the N_2 adsorption data as well as the ultramicropores (>0.7 nm) volume and width obtained for the analysis of the CO_2 adsorption data were included in Table 1. Pure CX present a S_{BET} of 712 m^2/g whereas Fe-doped samples present a much smaller one of around 480 m^2/g. It is also noteworthy that the micropore width increases from 0.69 nm for CX sample to 1.34–1.76 nm for Fe-doped CX ones. This microporosity decrease and widening is also accompanied by an increase of the mesoporosity; V_{meso} increases with the increase of Fe content in FeCX-Y samples. Overall, the microporosity (W_0 (N_2)) and ultramicroporosity (W_0 (CO_2)) decreases for Fe-doped CX samples regarding the CX counterpart at the expense of an increase in the mesoporosity (V_{meso}).

3.3. XRD and Raman spectroscopy

The graphitization degree of FeCX-Y pointed out by HRTEM was corroborated by XRD and Raman spectroscopy results (Figs. 4 and 5 and Table 2). XRD diffractogram of CX sample reveals two intense peaks at $2\theta = 22.0°$ and 43.8° ascribed to the graphite (002) and (100) planes, respectively (JCPDS # 89–8487). A shoulder at 26.0° appears and the peak at 43.8° moves to lower 2θ angles for FeCX-Y. This new sharp peak and the displacement increases by increasing the % Fe in the FeCX-Y being predominant for FeCX-0.8 sample. This (002) and (100) peak displacement denotes the presence of new structures with lower d-spacing and so, could be attributed to the development of graphitic clusters by increasing the Fe content as it was pointed out by HRTEM.

Bragg's equation (6)(Qiu et al., 2019) was applied to obtain the interlayer spacing (d_{002}):

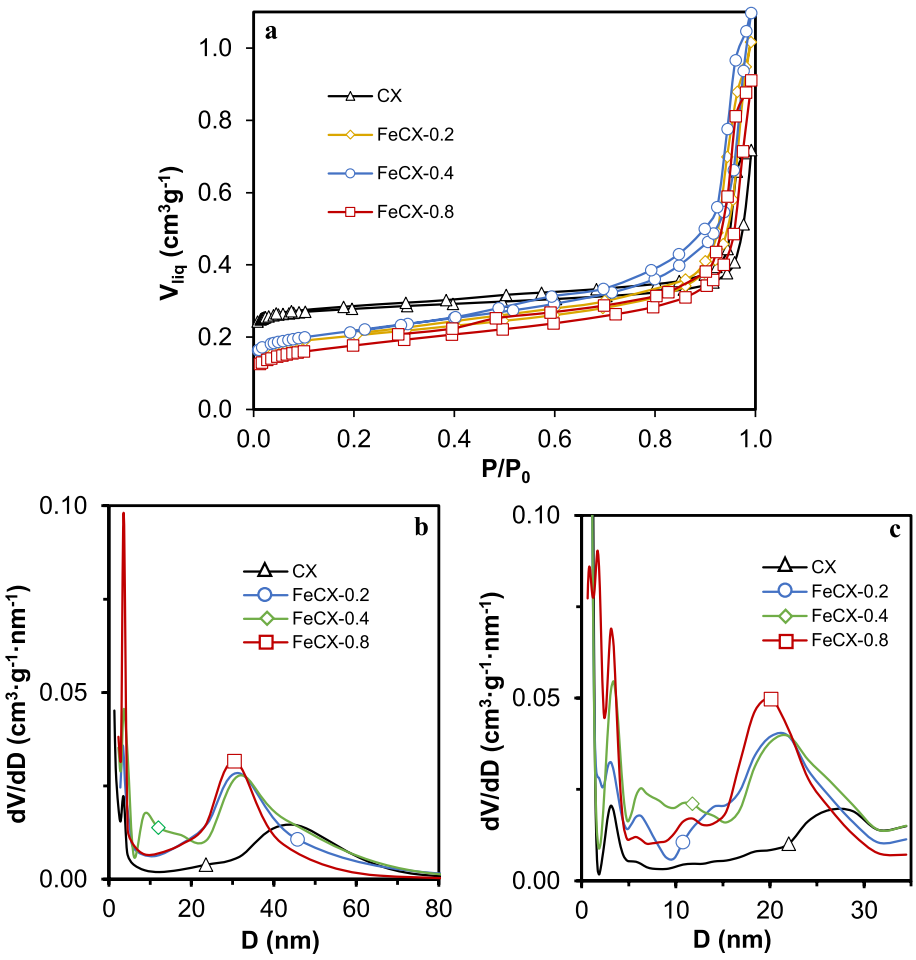

Fig. 3. N_2 isotherms at −196 °C (a) and BJH (b) and QSDFT (c) pore size distribution of pure (CX) and Fe-doped (FeCX-Y) carbon samples.

Table 1
Porous textural properties of the pure and Fe-doped carbon xerogels and the total metal content determined by TGA (M_{TGA}) and ICP-OES (M_{ICP}).

Sample	N_2-isotherm					CO_2-isotherm			
	S_{BET}	W_0	L_0	$V_{0.95}$	V_{MESO}	W_0	L_0	M_{TGA}	M_{ICP}
	$m^2\ g^{-1}$	$cm^3\ g^{-1}$	nm	$cm^3\ g^{-1}$		$cm^3\ g^{-1}$	nm	wt. %	wt. %
CX	712	0.274	0.69	0.407	0.132	0.315	0.60	–	–
FeCX-0.2	487	0.208	1.47	0.699	0.491	0.289	0.59	0.21	0.24
FeCX-0.4	480	0.209	1.34	0.776	0.567	0.259	0.60	0.42	0.45
FeCX-0.8	404	0.177	1.76	0.811	0.634	0.195	0.64	0.83	0.80

$$d_{(002)} = \frac{\lambda}{2 \sin \theta_{(002)}} \quad (6)$$

where λ is the X-ray radiation wavelength (1.54056 Å) and θ is the diffraction peak Bragg angle. The obtained results were collected in Table 2. Note that $d_{(002)}$ decreases with the increase of Fe content being the value for FeCX-0.8 (≈0.3458 nm) very close to ideal graphite crystal layer spacings (0.3354 nm) manifesting the high graphitization degree of FeCX-Y samples regarding the CX counterpart (0.4008 nm).

Note also that new but low intense peaks appear at 2θ = 30.6° and 35.7° in FeCX-Y samples which could be attributed to Fe_3O_4 spinel (JCPDS # 75–0033). The presence of Fe^0 cannot be ruled out as the more intense diffraction peak of Fe^0 (100) overlaps with (100) graphite plane. Moreover, XRD data reflects that small Fe crystal size (<20 nm, Table 2) were obtained, implying that the Fe particles are well dispersed throughout the carbon matrix corroborating the HRTEM observations. It is also important to highlight that despite the organic gels were carbonized at 800 °C in inert atmosphere and H_2 can be also produced during this pyrolysis, oxidized Fe is detected instead of metallic Fe which would be more expected. This oxidized phase can be ascribed to the surface oxidation of iron particles after the exposure of samples to the atmosphere.

The formation of graphitic clusters catalyzed by the Fe phase was again confirmed by Raman spectroscopy (Fig. 5). I_D/I_G ratio (I_D and I_G are the defect band and graphitization band intensity, respectively) is usually considered as an indicator of the carbon structural ordering, as much lower is this ratio much higher is the graphitization degree (Wang et al., 1990). Nonetheless, the I_D/I_G ratio does not depend only on the graphitization degree but also on the crystallite size being inversely proportional to the crystallite size forming the graphite-like carbons (Ferrari, 2007). Therefore, D and G bandwidth (W) must be also taking into account to characterize the graphitic structure of carbon materials (Vallerot et al., 2006). In this sense, a wide G band indicates a more disordered structure (by disorientations and/or in-plane defects)

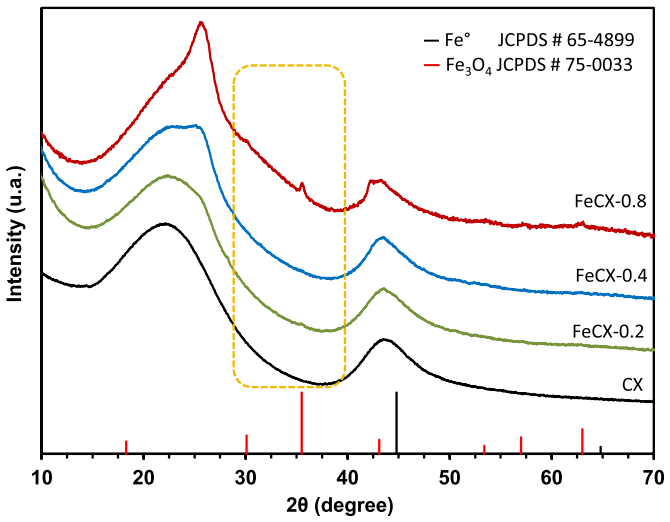

Fig. 4. XRD patterns of pure (CX) and Fe-doped (FeCX-Y) carbon samples.

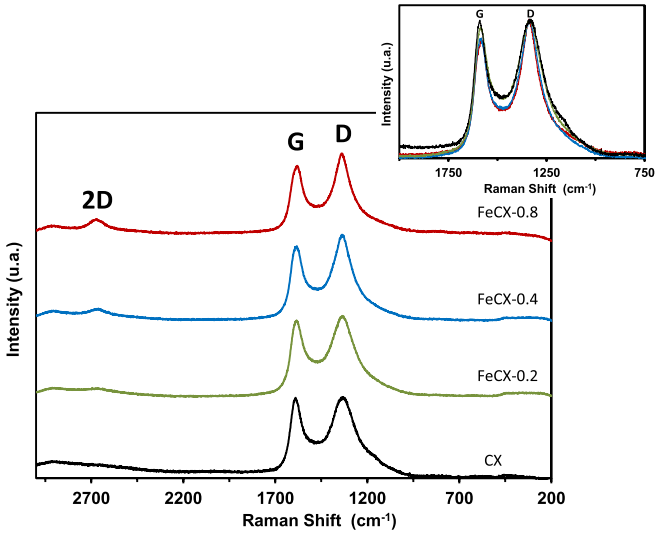

Fig. 5. Raman spectra of pure (CX) and Fe-doped (FeCX-Y) carbon samples.

Table 2
Crystal size of Fe particles (D_{Fe}) and graphitic phase interlayer spacing (d_{002}). Raman intensity ratio (I_D/I_G) and D band Width (W_D).

Sample	XRD (nm)		Raman	
	$d_{(002)}$	D_{Fe}	I_D/I_G	W_D (cm^{-1})
CX	0.4008	–	1.01	185.7
FeCX-0.2	0.3945	n.d.[a]	1.03	176.3
FeCX-0.4	0.3506	n.d.[a]	1.09	141.1
FeCX-0.8	0.3458	19.7	1.09	118.3

[a] Fe peak was not resolved enough to apply the Scherrer eq.

(Vallerot et al., 2006). Thus, a narrower W_D and lower I_D/I_G ratio denotes a higher graphitization degree.

Note that Raman results are in accordance with XRD conclusions. Raman spectra of pure CX and FeCX-0.2 are similar; nonetheless, the D band becomes sharper and narrower by increasing the Fe content in the sample revealing an enhancement of graphitization in that sense. Note also that the 2D peak intensity increases with the Fe content. The emergence of the 2D Raman band is characteristic for graphite which corroborates the increase of the graphitization degree (Schuepfer et al., 2020). I_D/I_G ratio and W_D width are collected in Table 2. I_D/I_G ratio is very similar in all samples but since it is affected by the crystallite size and it seems to increase with Fe content (XRD peaks becomes sharper and narrower, see XRD results), that should not be considered as similar graphitization degrees of the samples. As it was commented above, D band Width (W_D) need to be considered in order to well characterize the graphitization degree of samples. Note that the W_D decreases by increasing the Fe content in the samples corroborating again an enhancement of the degree of graphitization in this sense.

3.4. TGA and XPS

The real content of Fe in FeCX-Y carbon samples and its distribution on the carbon gel surface was determined by TGA and ICP-OES and XPS, respectively. C_{1s}, O_{1s} and Fe_{2p} regions are depicted in Fig. 6 and data collected in Table 2. TGA data shows than the thermal stability of samples (Fig. S1) is not affected by the presence of iron in the carbon matrix and the real Fe content obtained by burning the carbon phase and also by ICP-OES is very close to the theoretical one.

Regarding XPS, note that Fe signal (Fig. 6c) is not or slightly detected in Fe-doped carbon gels which manifests that most of the metal particles, as it was observed by HRTEM, are embedded by the carbon matrix. The increase of the graphitization of samples is also pointed out by analyzing de C_{1s} spectral region. The FWHM of the C═C peak can be related, together with other factors, with the graphitic ordering, so a low FWHM could indicate a high crystallinity (Jiménez Mateos and Fierro, 1996; Takahagi and Ishitani, 1988). The C_{1s} region spectra is depicted in Fig. 6a. Six peaks were needed to deconvolve the C_{1s} region which are assigned to C═C (284.6 eV), C–C (285.5 eV), C–O (286.5 eV), C═O (287.8 eV), O═C-OR (289.3 eV) bonds and a satellite peak of π–π* (291.0 eV). This region is very similar for both pure and Fe-doped carbon xerogels denoting a similar surface chemistry but the FWHM of the C═C peak clearly decreases by increasing the Fe content in the carbon matrix (Table 3) which can be ascribed to the increase of the graphitic ordering induced by the presence of Fe nanoparticles.

With regards to O_{1s} region (Fig. 6b), two peaks at 532.1 and 533.5 are observed in pure CX carbon xerogel (Table 3) attributed to C═O and C–O bonds, respectively. In Fe-doped carbons (FeCX-Y samples), a third peak is also needed at 530.6 eV which is attributed to Fe–O bonds. It is important to highlight that this contribution is not very significant because of the low metal content and, as HRTEM images pointed out, most of Fe particles are embedded by the carbon matrix. Nonetheless, this contribution increases with the increase of the amount fe in the carbon matrix. The oxygen content of all carbons is very similar (around 8%) which indicates that the Fe-doping does not highly affect the surface chemistry.

3.5. Oxygen reduction reaction

The ORR activity was studied using a rotating ring-disk electrode (RRDE). CVs were performed while N_2 or O_2 were bubbling through a 0.1 M KOH solution and data are depicted in Figs. 7 and 8. The different electrochemical behavior of samples in N_2 bubbling (Fig. 7) can be related to the different conductivity/graphitization degree and textural properties of samples since all samples have almost the same oxygen content (around 8 wt %, see XPS). The area enclosed in the CVs, that is the capacitance, decreases in Fe-doped CX samples regarding the CX counterpart due to mainly the high decrease of microporous surface where the electric double layer is formed. The S_{BET} and W_0 (N_2) is reduced by almost half by the Fe-doping (Table 2) and consequently, the capacitance decreases. It is known that optimum specific capacitance is achieved with pore ranging in 0.7–1 nm whereas pores smaller than 0.5 nm are too narrow for the diffusion of the electrolyte and the double layer formation (Rufford et al., 2009; Vallerot et al., 2006). In contrast, although the contribution of mesopores (2−50 nm) to the double layers is not as high that of the micropores, such mesoporosity can improve the

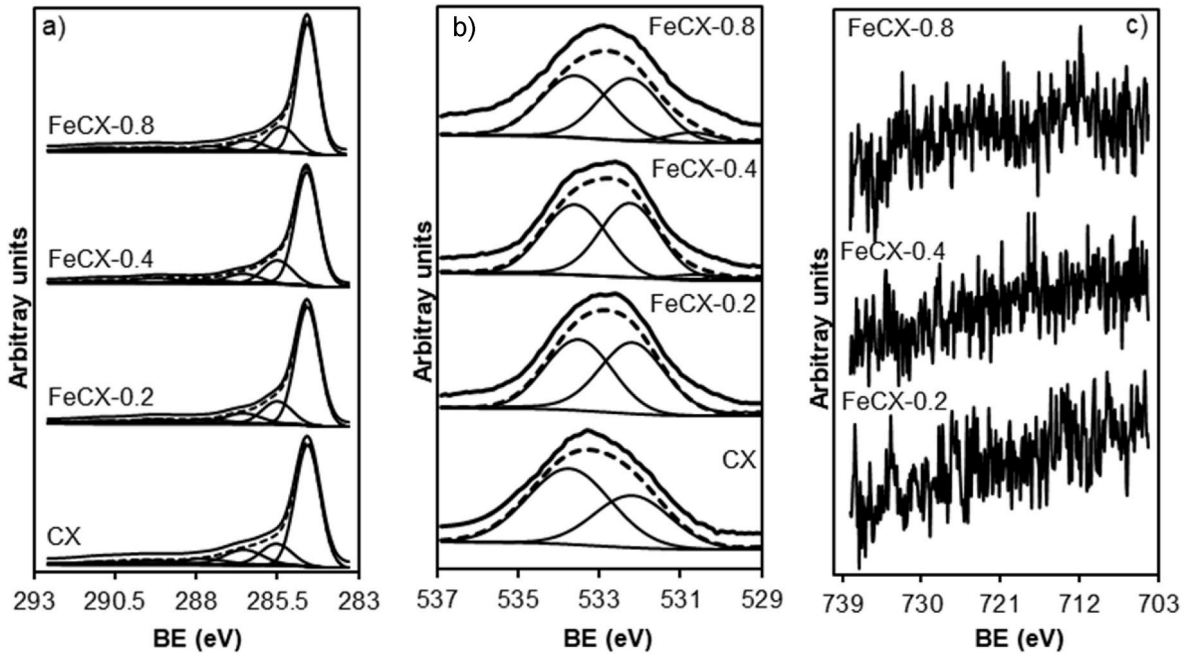

Fig. 6. XPS patterns of the a) C_{1s}, b) O_{1s} and Fe_{2p} regions.

Table 3
Surface chemical composition determined by XPS and the total iron content obtained by TGA (Fe_{TGA}).

Sample	C_{1s}				O_{1s}				Fe_{TGA} (%)
	B.E (eV)	Assign.	FWHM (eV)	Peak (%)	B.E (eV)	Assign.	Peak (%)	O (%)	
CX	284.6	C=C	0.92	63	532.2	O=C	38	7.6	–
	285.5	C–C		13	533.8	O–C	62		
	286.5	C–O		11					
	287.8	C=O		5					
	289.4	COO^-		4					
	290.9	π−π*		3					
FeCX-0.2	284.6	C=C	0.88	66	532.2	O=C	51	**7.5**	**0.21**
	285.5	C–C		15	533.5	O–C	49		
	286.6	C–O		8					
	287.8	C=O		4					
	289.3	COO^-		4					
	290.9	π−π*		2					
FeCX-0.4	284.6	C=C	0.85	65	530.6	O–Fe	3	**7.9**	**0.42**
	285.4	C–C		16	532.3	O=C	49		
	286.4	C–O		8	533.6	O–C	48		
	287.6	C=O		4					
	289.2	COO^-		4					
	291.0	π−π*		2					
FeCX-0.8	284.6	C=C	0.76	65	530.7	O–Fe	6	**7.0**	**0.83**
	285.4	C–C		16	532.3	O=C	45		
	286.4	C–O		8	533.6	O–C	49		
	287.6	C=O		3					
	289.2	COO^-		4					
	291.0	π−π*		3					

EDLC formation at fast charge rates due to enhancement of the electrolyte diffusion through the carbon network to the micropores active sites. Note that despite de surface area slightly decreases and the micropore width increases by increasing the Fe content, the CV enclosed area (that is the capacitance) is constant or even increases for FeCX-0.8 (the sample with lower surface area, 400 m^2/g, and widest micropores, 1.76 nm). This slightly improve of capacitance by increasing the Fe content can be explained based to the better electrolyte diffusion due to the increase of the mesopore volume and/or the enhancement of the conductivity/graphitization degree of samples. It is known that the enhancement of the electrical conductivity results in a marked improvement of both the energy, power densities and specific capacitance (Ramos-Fernández et al., 2018).

The CV voltammograms in N_2 and O_2-saturated electrolyte were depicted in Fig. 8. An intense current intensity increment is observed for all samples at around −0.20 V vs Ag/AgCl in presence of O_2 regarding the N_2 counterpart, which manifests that all prepared carbon xerogels are active in the ORR. Nonetheless, despite CVs tests indicates activity of all samples, the Fe content seems to affect the achieved current density at the same potential and probably also the number of electrons transferred. It is important to highlight that at higher Fe contents (0.4 and 0.8%) a reduction peak is observed both in N_2 and O_2 saturated electrolyte at around −0.4 V vs Ag/AgCl attributed to the Fe species redox process (Alves et al., 2019; Doménech et al., 2002; Lin et al., 2021; Radhi

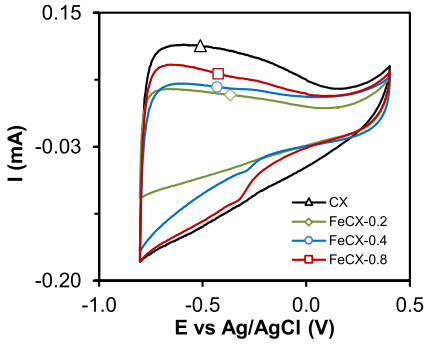

Fig. 7. Cyclic voltammogram in N_2-saturated KOH solution at 1000 rpm and 50 mV/s.

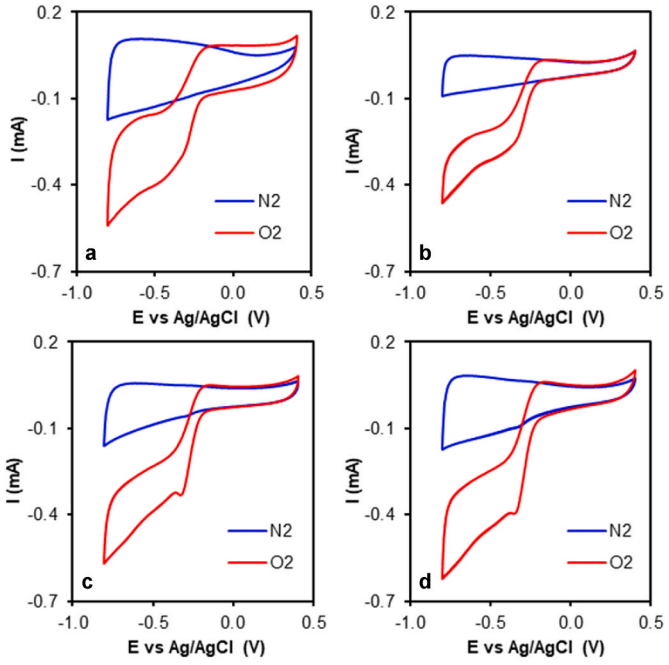

Fig. 8. Cyclic voltammograms at 1000 rpm and 50 mV/s of a) CX, b) FeCX-0.2, c) FeCX-0.4 and d) FeCX-0.8 in N_2 bubbling (blue line) and O_2 bubbling (red line) KOH solution.

et al., 2014). At potentials below −0.45 V vs Ag/AgCl, Fe^{2+} ions are reduced to Fe^0 in aqueous solutions (Doménech et al., 2002; Radhi et al., 2014).

For further details, the corresponding Linear Sweep Voltammetries (LSV) were obtained at different rotation speeds (Fig. 9a and **b**), and data were adjusted to the Koutecký–Levich equation (Fig. 9c and **d**) to evaluate the number of electrons transferred (n) at different potentials (Fig. 9e) and the kinetic density current (jk) (Table 4). As expected, the current intensity increased by increasing the rotation speed form 500 rpm–3500 rpm due to the reduction of diffusion limitations (Fig. 9a). The linearity of the K-L plots in all samples denotes a first-order reaction kinetics toward the concentration of dissolved oxygen (Fig. 9c and **d**). The fitting lines are completely parallel for CX sample (Fig. 9c) which indicates that the electron transfer numbers for ORR do not change with the potentials, however a change of slope occurs at −0.4/-0.5 V for FeCX-Y samples (e.g. FeCX-40 sample, Fig. 9d) manifesting an increase of the electrons transferred at potential higher than −0.5 V. This fact was confirmed analyzing the number of electrons transferred (Fig. 9e) at different potentials. All materials catalyze the oxygen reduction reaction via the 2-electron route with an onset potential of around −0.21 V vs Ag/AgCl (Table 4). Note that the presence of Fe considerably improves

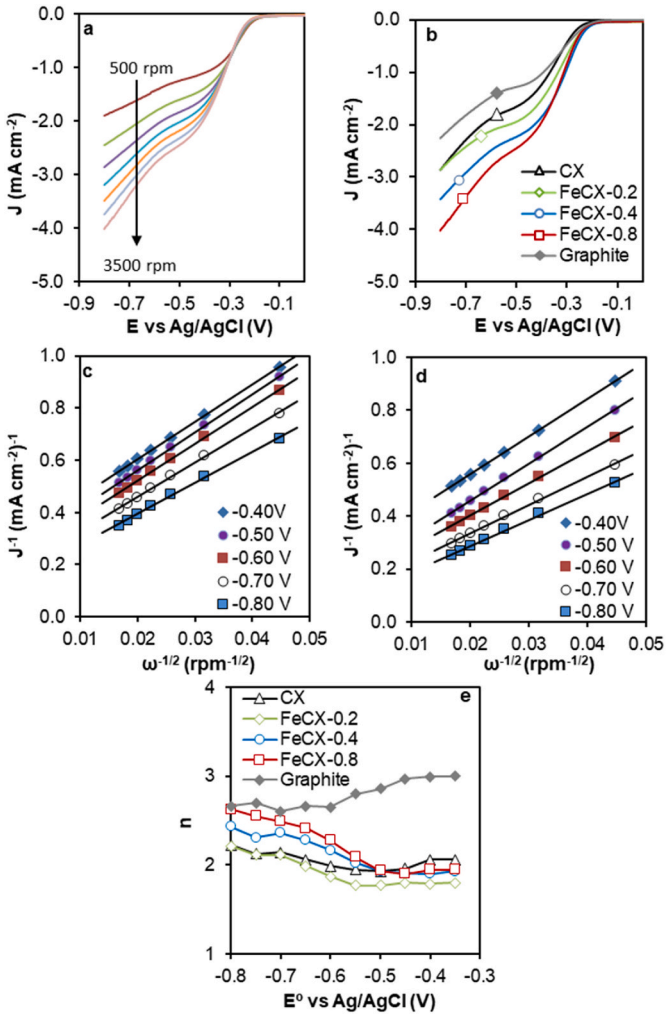

Fig. 9. LSV curves for FeCX-0.8 sample at different RRDE rates (a) and all samples at 3500 rpm (b). K-L plot of CX (c) and FeCX-0.8 (d) samples, e) number of electrons transferred at each potential for all samples. Data obtained from the disc electrode.

Table 4
Electrochemical parameters obtained from the analysis of LSV curves.

Sample	E_{ONSET} (V)	[a] j_k / mAcm^{-2}	n
CX	−0.23	6.46	2.2
FeCX-0.2	−0.23	6.47	2.2
FeCX-0.4	−0.22	9.91	2.4
FeCX-0.8	−0.20	11.11	2.6

[a] J_k and n refer to K-L fitting at −0.8 V (vs. Ag/AgCl).

the electro-catalytic activity (jk values in Table 4) which can be attributed to the enhanced graphitization degree/conductivity and thus, a faster charge transfer that improves the ORR efficiency. However, for samples without Fe (CX) or with low amount of Fe (FeCX-0.2) the electron transferred (n) is around 2 and remains invariable at increasing potentials, whereas for samples with higher Fe content (FeCX-0.4 and FeCX-0.8), n remains constant up to −0.5 V and then slightly increases. This increase can be explained based on the presence of Fe and the redox processes observed in CVs. As it was commented in characterization section, despite Fe^0 cannot be ruled out, Fe_3O_4 is the main crystalline phase detected. These oxidized Fe species ($Fe^{\delta+}$) are reduced at −0.4 eV given redox processes that increases the total electron transferred.

Moreover, the O_2 interaction strength with the metallic phase obtained by the reduction of Fe oxidized species could be higher affecting the selectivity to ORR. The key factor for assess the 2-electron pathway is the active site-O species interaction. An enough strong interaction to overcome the reaction barrier is required but not too strong in order to prevent the O–O bond dissociation that favors the selectivity towards H_2O (Kulkarni et al., 2018b) This interaction active site-O and thus, the ORR selectivity, depend on different factors including the type of transition metal (Wu and Xu, 2018a; Xu et al., 2015) and its oxidation state (Qin et al., 2022; Toh et al., 2015). Therefore, the activity and selectivity of ORR is mainly affected by the electronic interaction of the intermediates with the metal atoms. Several authors have demonstrated that the ORR activity and selectivity depend on the binding strength of the key reaction intermediate, *OOH (Jiang et al., 2019b). The O–O bond dissociation is enhanced when a strong *OOH adsorption energy on the catalysts surface, thus the 4e-pathway with H_2O as the major product is achieved (Chen et al., 2018; Jiang et al., 2019b; Lu et al., 2018; Siahrostami et al., 2013). Kun Jiang et al. (2019b) studied the control of the ORR selectivity using Fe single atom in CNT and pointed out that *OOH generally binds too strong at Fe sites leading to dissociation of the O–O bond dissociation. However, the introduction of oxygen into catalysts causes most of the C atoms in the vicinity of the Fe–C–O motifs to show a high activity for H_2O_2 production. Quiowan Chang et al. (2020) also showed that metal-oxygen coordination introduces efficient active sites for the 2e− ORR. They studied partially oxidized Pd clusters on enhancing 2e− ORR activity, so $Pd^{\delta+}$-OCNT electrocatalysts were prepared and tested in ORR in comparison with mild thermal annealing (450 °C for 5 h) Pd-OCNT sample observing that for $Pd^{\delta+}$-OCNT electrocatalyst is almost exclusively selective toward the 2e-pathway whereas for the Pd-OCNT catalyst, the reduction of O_2 to H_2O is preferred. Therefore, they conclude that the partially oxidized Pd clusters are crucial for the enhancement of the activity and high selectivity for H_2O_2 production. That could explain the change of selectivity observed at potential higher than −0.5 eV. At potential lower than −0.5 eV, the present of $Fe^{\delta+}$ species or even Fe–O–C active sites favour the selectivity to 2e-pathway, however at potential higher than −0.5 eV, $Fe^{\delta+}$ species are reduced favoring a O–O strong interaction enhancing the 4e-pathway.

The number of electrons transferred, and the hydrogen peroxide production were also studied by analyzing the ring electrode data (Fig. 10). Note that similar conclusions that of the obtained with the disc electrode are achieved. The number of electrons transferred is near to 2 in all samples at potential lower than −0.5 eV producing around 70–80% of H_2O_2. At potential higher than −0.5, while for the Fe-undoped sample (CX) n and % H_2O_2 remain constant, n increases and consequently %H_2O_2 decreases for the Fe-doped ones (FeCX-Y) denoting a change in the nature of Fe-based active sites, as commented above.

It is important to highlight that despite the slightly change of selectivity observed at −0.5 eV potential in Fe-doped samples, number of electrons transferred is near to 2 in all samples and in all potential range with a production of H_2O_2 higher than 65% with the advantage that the presence of Fe enhances the electron conductivity of samples favoring the ORR performance. Overall, the introduction of the Fenton active site (Fe) as doping agent during the synthesis of carbon xerogels enhances the electron conductivity of samples improving the ORR performance and controls the Fe-oxygen interaction favoring the 2e-pathway. Therefore, Fe-doped carbon xerogels are presented as good candidates to act as bifunctional electro-Fenton catalysts for the *in-situ* generation of H_2O_2 and for the generation of hydroxyl radicals from the generated H_2O_2.

3.6. Electro-fenton degradation of tetracycline

Based on the ORR results, FeCX-0.8 sample was selected for the electro-Fenton degradation test since it presents the highest activity (see jk values) and a high selectivity to H_2O_2 production. For the electro-Fenton test, tetracycline (TTC) was selected as target drug and the potential was fixed in −0.6 eV to maintain a high H_2O_2 selectivity with a high activity. The electrode was previously saturated with the drug in the dark to remove the adsorptive performance of each sample from the degradation tests. After saturation, the initial TTC concentration (C_0) was fitted to 10 mg L^{-1}, and then, the selected voltage was applied. This time was considered as the start degradation time. Since electrodes were prepared by pasting the sample on a graphite sheet, this graphite sheet was also tested in the electro-Fenton and used as reference. The degradation curve of FeCX-0.8 is depicted in Fig. 11 in comparison with the CX sample and graphite sheet used as references. Note that CX sample shown degradation (50% after 7 h) despite Fenton active phase is not present in this sample. This activity could be explained based on the direct oxidation of TTC by the H_2O_2 electrogenerated by CX sample (see ORR results), the electrochemical oxidation or reduction of TTC on the electrodes or by radical obtained (·OH) by the electrochemical reduction of O_2 via overall 3-electron pathway (eq. (6)) (NOE et al., 2012; Xiao et al., 2021) or by electrocatalytic reduction of the generated H_2O_2 via 1-electron pathway (eq. (7)) (NOE et al., 2012). Therefore, in order to explain this unexpected electro-Fenton activity of CX sample, several experiences were performed. In the first one, 350 ppm of H_2O_2 (30 w. t. %) was added to a solution of 10 ppm of TTC without any catalyst in order to discard TTC degradation by oxidation with H_2O_2, however activity was not observed. To discard the direct TTC oxidation or

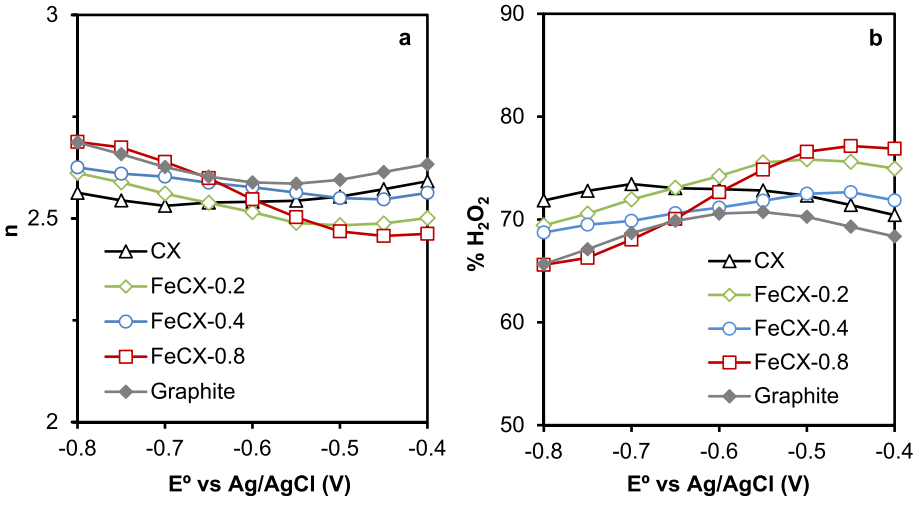

Fig. 10. Number of electrons transferred (a) and the % H_2O_2 produced (b) at each potential for all samples. Data obtained from the ring electrode.

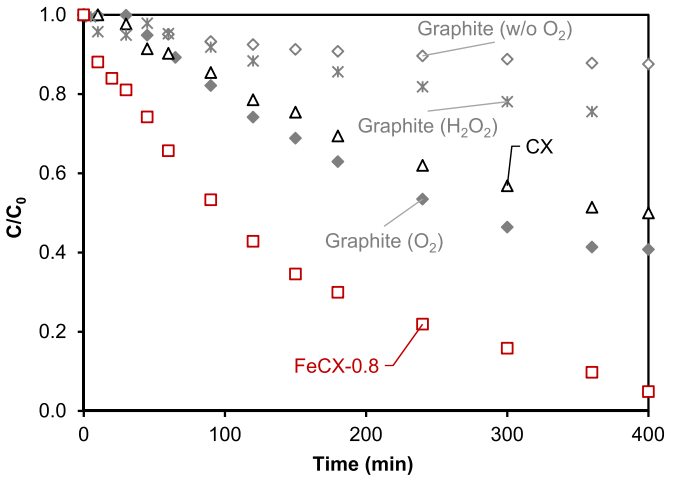

Fig. 11. Normalized TTC concentration (C/C_0) vesus time for EF tests at potential of −0.60 V for undoped carbon xerogel (CX), Fe-doped carbon xerogel (FeCX-0-4) and graphite sheet reference (Graphite (O_2)) under O_2 bubbling. Electro-Fenton tests were also performed without bubbling O_2 in absence (Graphite (w/o O_2)) or in presence (Graphite (H_2O_2)) of H_2O_2 (350 ppm) using graphite reference.

reduction on the electrodes, graphite sheet was used as electrode in presence and absence of O_2 bubbling. In absence of O_2 bubbling, the activity is not so high (less than 12%), whereas around 60% of degradation was obtained in presence of O_2. This corroborates that O_2 is required for the degradation of tetracycline and, therefore, the TTC degradation is explained by the directly generated ·OH radicals by the electrochemical reduction of O_2 or H_2O_2. Since the number of electrons transferred in the ORR for graphite is near to 3 (see Figs. 9 and 10), this seems to indicate that the OH· radicals come from the electroreduction of O_2 via 3-electron pathway. To corroborate this, an electro-Fenton test was also performed using graphite sheet as electrode in a solution saturated with N_2 and with 450 ppm of H_2O_2. The activity does not increases too much in presence of H_2O_2 (absence of O_2), from 12% without O_2 and H_2O_2 to 21% with H_2O_2, which indicates that despite the production of OH· radicals by the electroreduction of H_2O_2 seem to be also present but in low extend, the main reason of de TTC degradation in the Fenton-type metal-free catalysts (graphite and CX) is the electro-generation of OH· radicals by the electroreduction of O_2 via 3-electron pathway.

$$O_2 + 2H^+ + 3e^- \rightarrow OH^- + OH^\bullet \quad (7)$$

$$H_2O_2 + e^- \rightarrow OH^- + OH^\bullet \quad (8)$$

If a Fenton catalyst (Fe) is present in the carbon matrix (CX), FeCX-0.8, almost total TTC degradation (95.13%) is achieved after 7 h of reaction without the use of any external Fenton-catalysts. This manifests that the presence of Fe on the CX matrix favors the OH· radicals production increasing the electro-Fenton activity and thus, the TTC degradation. Overall, Fe-doped carbon xerogels are presented as excellent dual-functional electro-Fenton catalysts to perform both the electroreduction of O_2 to H_2O_2 and Fenton for it use in wastewater decontamination. Finally, the Fe leaching was analyzed by atomic absorption spectroscopy and there was no Fe ion leaching with any catalyst.

Overall, the synthesized dual-functional Fe-doped carbon xerogel based cathodes provides a promising, efficient and facile Electro-Fenton advanced oxidation process for the decontamination of emerging-polluted water streams before being discharged into various ecosystems.

4. Conclusions

The Electro-Fenton process requires the use of two catalysts: one acting as electrocatalyst for the reduction of oxygen to H_2O_2 and another Fenton-type catalyst for the generation of ·OH radicals from H_2O_2. Thus, the search of materials with dual functionality for the electro-reduction of oxygen to H_2O_2 and Fenton is a hot research issue in the last years. However, the preparation of heterogeneous EF catalysts with high selectivity and activity towards ORR via the two-electron pathway is challenging, since the active sites for Fenton are mainly transition metals that in the main catalyze oxygen reduction via the 4e-pathway. With this aim, highly graphitic Fe-doped carbon xerogels were synthesized in this manuscript by sol-gel polymerization of resorcinol and formaldehyde as dual-functional electro-Fenton catalysts for wastewater decontamination. The amount of Fe introduced was optimized in order to control the O_2-catalyst interaction to maximize the H_2O_2 production and its transformation into $OH^\bullet$ radicals for tetracycline degradation. The following conclusions have been achieved.

- The presence of Fe affects the RF polymerization; The undoped sample present a S_{BET} of 712 m^2/g whereas Fe-doped samples present a much smaller one of around 480 m^2/g. The microporosity decreases and become wider and the V_{meso} increases with the increase of Fe content in FeCX-Y samples. Overall, the microporosity (W_0 (N_2)) and ultramicroporosity (W_0 (CO_2)) decreases for Fe-doped CX samples regarding the CX counterpart at the expense of an increase in the mesoporosity (V_{meso}).
- Graphitic clusters are clearly identified in Fe-doped samples by HRTEM while they are not present in undoped CX. The amount of those graphitic clusters increases with the increase of the Fe content of the samples (FeCX-0.2 < FeCX-0.4 < FeCX-0.8); at content as low as 0.8% the sample is almost entirely composed of such clusters.
- The graphitization degree of FeCX-Y observed by HRTEM was corroborated by XRD and Raman spectroscopy results. The XRD peaks at $2\theta = 22.0°$ and 43.8° ascribed to the graphite planes become sharper and move to lower 2θ angles by increasing the % Fe in the FeCX-Y being predominant for FeCX-0.8 sample. This peak displacement denotes the development of new structures with lower d-spacing and so, could be attributed to the development of graphitic clusters by increasing the Fe content as it was pointed out by HRTEM. The d (002)-spacing decreases with the increase of Fe content being the value for FeCX-0.8 (≈0.3458 nm) very close to ideal graphite crystal layer spacings (0.3354 nm) manifesting the high graphitization degree of FeCX-Y samples regarding the CX counterpart (0.4008 nm). Analyzing Raman spectra, the D band becomes sharper and narrower by increasing the Fe content in the sample indicating an increase of graphitization in that sense. The 2D peak intensity also increases with the Fe content.
- The presence of Fe considerably improves the electro-catalytic activity (j_k values) due to the enhanced graphitization degree/conductivity. However, a chance of mechanism seems to occur at around −0.5 V for samples with high amount of Fe (electron transferred (n) increases). At potential lower than −0.5 eV, the present of $Fe^{\delta+}$ species or even Fe–O–C active sites favour the selectivity to 2e-pathway, however at potential higher than −0.5 eV, $Fe^{\delta+}$ species are reduced favoring a O–O strong interaction enhancing the 4e-pathway.
- Based on the ORR results, FeCX-0.8 sample was selected for the electro-Fenton degradation test using tetracycline (TTC) as target drug. The CX sample shown degradation (50% after 7 h) despite Fenton active phase is not present in this sample. This activity was explained based on the direct generation of OH· radicals by the electroreduction of O_2. Almost total TTC degradation (95.13%) is achieved after 7 h of reaction for FeCX-0.8 sample because of the Fe on the CX matrix favors the OH· radicals production increasing the electro-Fenton activity and thus, the TTC degradation. Therefore, Fe-doped carbon xerogels are presented as excellent dual-functional electro-Fenton catalysts to perform both the electro-reduction of O_2 to H_2O_2 and Fenton for it use in wastewater decontamination.

Credit author statement

A. Barranco-López: Investigation. A.I. Moral-Rodríguez: Investigation, Conceptualization, Formal analysis, Supervision. E. Fajardo-Puerto: Investigation, Formal analysis. A. Elmouwahidi: Methodology, Investigation. E. Bailón-García: Conceptualization, Methodology, Formal analysis, Writing – original draft preparation, Funding acquisition

Declaration of competing interest

The authors declare that they have no known competing financial interests or personal relationships that could have appeared to influence the work reported in this paper.

Data availability

Data will be made available on request.

Acknowledgments

This research has been supported by the Spanish Project PID2021-127803OB-I00 funded by MCIN/AEI/10.13039/501100011033/ and by "ERDF A way of making Europe"and Junta de Andalucía (P18-RTJ-2974 and B. RNM.566. UGR20). Authors also thanks the "Unidad de Excelencia Química Aplicada a Biomedicina y Medioambiente" of the University of Granada (UEQ - UGR) for its technical assistance. E. Bailón-García is grateful to MINECO for her postdoctoral fellowship (RYC 2020-029301-I).

Appendix A. Supplementary data

Supplementary data to this article can be found online at https://doi.org/10.1016/j.envres.2023.115757.

References

Alothman, Z.A., 2012. A review: fundamental aspects of silicate mesoporous materials. Materials 5, 2874–2902. https://doi.org/10.3390/ma5122874.

Alves, I.C.B., Santos, J.R.N., Viégas, D.S.S., Marques, E.P., Lacerda, C.A., Zhang, L., Zhang, J., Marques, A.L.B., 2019. Nanoparticles of Fe2O3 and Co3O4 as efficient electrocatalysts for oxygen reduction reaction in acid medium. J. Braz. Chem. Soc. 30, 2681–2690. https://doi.org/10.21577/0103-5053.20190195.

Ameta, R., Chohadia, K., Jain, A., Punjabi, P.B., 2018. Chapter 3 - Fenton and photo-fenton processes. In: Ameta, S.C., Ameta, R. (Eds.), Advanced Oxidation Processes for Waste Water Treatment. Academic Press, pp. 49–87. https://doi.org/10.1016/B978-0-12-810499-6.00003-6.

Belgiorno, V., Rizzo, L., Fatta, D., Della, C., 2007. Review on endocrine disrupting-emerging compounds in urban wastewater : occurrence and removal by photocatalysis and ultrasonic irradiation for wastewater reuse. Desalination 215, 166–176. https://doi.org/10.1016/j.desal.2006.10.035.

Brillas, E., Sirés, I., Oturan, M.A., 2009. Electro-fenton process and related electrochemical technologies based on fenton's reaction chemistry. Chem. Rev. 109, 6570–6631.

Castelo-Quibén, J., Abdelwahab, A., Pérez-Cadenas, M., Morales-Torres, S., Maldonado-Hódar, F.J., Carrasco-Marín, F., Pérez-Cadenas, A.F., 2018. Carbon - iron electro-catalysts for CO2 reduction. The role of the iron particle size. J. CO2 Util. 24, 240–249. https://doi.org/10.1016/j.jcou.2018.01.007.

Chang, Q., Zhang, P., Hassan, A., Mostaghimi, B., Zhao, X., Denny, S.R., Lee, J.H., Gao, H., Zhang, Y., Xin, H.L., Siahrostami, S., Chen, J.G., Chen, Z., 2020. Promoting H2O2 production via 2-electron oxygen reduction by coordinating partially oxidized Pd with defect carbon. Nat. Commun. 11, 2178. https://doi.org/10.1038/s41467-020-15843-3.

Chen, Chen-yu, Tang, C., Wang, H., Chen, Cheng-meng, Zhang, X., Huang, X., Zhang, Q., 2016. Oxygen reduction reaction on graphene in an electro- Fenton system : in situ generation of H2O2 for the oxidation of organic compounds. ChemSusChem 9, 1194–1199. https://doi.org/10.1002/cssc.201600030.

Chen, S., Chen, Z., Siahrostami, S., Kim, T.R., Nordlund, D., Sokaras, D., Nowak, S., To, J. W.F., Higgins, D., Sinclair, R., Nørskov, J.K., Jaramillo, T.F., Bao, Z., 2018. Defective carbon-based materials for the electrochemical synthesis of hydrogen peroxide. ACS Sustain. Chem. Eng. 6, 311–317. https://doi.org/10.1021/acssuschemeng.7b02517.

Divyapriya, G., Nidheesh, P.V., 2020. Importance of graphene in the electro-fenton process. ACS Omega 5, 4725–4732. https://doi.org/10.1021/acsomega.9b04201.

Doménech, A., Pérez-Ramírez, J., Ribera, A., Mul, G., Kapteijn, F., Arends, I.W.C.E., 2002. Electrochemical characterization of iron sites in ex-framework FeZSM-5. J. Electroanal. Chem. 519, 72–84. https://doi.org/10.1016/S0022-0728(01)00724-0.

Ferrari, A.C., 2007. Raman spectroscopy of graphene and graphite: disorder, electron-phonon coupling, doping and nonadiabatic effects. Solid State Commun. 143, 47–57. https://doi.org/10.1016/j.ssc.2007.03.052.

Ghasemi, M., Khataee, A., Gholami, P., Soltani, R.D.C., Hassani, A., Orooji, Y., 2020. In-situ electro-generation and activation of hydrogen peroxide using a CuFeNLDH-CNTs modified graphite cathode for degradation of cefazolin. J. Environ. Manag. 267, 110629 https://doi.org/10.1016/j.jenvman.2020.110629.

Giordano, M., Barron, J., Olcay, U., 2019. Water scarcity and challenges for smallholder agriculture. Sustain. Food Agric. An Integr. Approach 75–94. https://doi.org/10.1016/B978-0-12-812134-4.00005-4.

Haider, M.R., Jiang, W.L., Han, J.L., Sharif, H.M.A., Ding, Y.C., Cheng, H.Y., Wang, A.J., 2019. In-situ electrode fabrication from polyaniline derived N-doped carbon nanofibers for metal-free electro-Fenton degradation of organic contaminants. Appl. Catal. B Environ. 256 https://doi.org/10.1016/j.apcatb.2019.117774.

Jiang, K., Back, S., Akey, A.J., Xia, C., Hu, Y., Liang, W., Schaak, D., Stavitski, E., Nørskov, J.K., Siahrostami, S., Wang, H., 2019a. Highly selective oxygen reduction to hydrogen peroxide on transition metal single atom coordination. Nat. Commun. 10, 3997. https://doi.org/10.1038/s41467-019-11992-2.

Jiang, K., Back, S., Akey, A.J., Xia, C., Hu, Y., Liang, W., Schaak, D., Stavitski, E., Nørskov, J.K., Siahrostami, S., Wang, H., 2019b. Highly selective oxygen reduction to hydrogen peroxide on transition metal single atom coordination. Nat. Commun. 10, 3997. https://doi.org/10.1038/s41467-019-11992-2.

Jiménez Mateos, J.M., Fierro, J.L.G., 1996. X-ray photoelectron spectroscopic study of petroleum fuel cokes. Surf. Interface Anal. 24 (199604), 223–236. https://doi.org/10.1002/(SICI)1096-9918.

Kulkarni, A., Siahrostami, S., Patel, A., Nørskov, J.K., 2018a. Understanding catalytic activity trends in the oxygen reduction reaction. Chem. Rev. 118, 2302–2312. https://doi.org/10.1021/acs.chemrev.7b00488.

Kulkarni, A., Siahrostami, S., Patel, A., Nørskov, J.K., 2018b. Understanding catalytic activity trends in the oxygen reduction reaction. Chem. Rev. 118, 2302–2312. https://doi.org/10.1021/acs.chemrev.7b00488.

Kumar, V., Ladha, J.K., 2011. Direct Seeding of Rice : Recent Developments and Future Research Needs, first ed. Elsevier Inc. https://doi.org/10.1016/B978-0-12-387689-8.00001-1. Advances in Agronomy.

Lata, S., Singh, P.K., Samadder, S.R., 2015. Regeneration of adsorbents and recovery of heavy metals: a review. Int. J. Environ. Sci. Technol. 12, 1461–1478. https://doi.org/10.1007/s13762-014-0714-9.

Li, G., Zhang, Y., 2019. Highly selective two-electron oxygen reduction to generate hydrogen peroxide using graphite felt modified with N-doped graphene in an electro-Fenton system. New J. Chem. 43, 12657–12667. https://doi.org/10.1039/c9nj02601k.

Li, Y., Cao, W.X., Zuo, X.J., 2022. O- and F-doped porous carbon bifunctional catalyst derived from polyvinylidene fluoride for sulfamerazine removal in the metal-free electro-Fenton process. Environ. Res. 212, 113508 https://doi.org/10.1016/j.envres.2022.113508.

Lin, X., Yang, F., You, L., xing, Wang, H., Zhao, F., 2021. Liposoluble quinone promotes the reduction of hydrophobic mineral and extracellular electron transfer of Shewanella oneidensis MR-1. Innovar 2, 100104. https://doi.org/10.1016/j.xinn.2021.100104.

Litter, M.I., Slodowicz, M., 2017. An overview on heterogeneous Fenton and photoFenton reactions using zerovalent iron materials. J. Adv. Oxid. Technol. 20, 20160164 https://doi.org/10.1515/jaots-2016-0164.

Lowell, S., Shields, J.E., Thomas, M.A., Thommes, M., 2004. Adsorption isotherms. In: Characterization of Porous Solids and Powders: Surface Area, Pore Size and Density, pp. 1–27.

Lu, Z., Chen, G., Siahrostami, S., Chen, Z., Liu, K., Xie, J., Liao, L., Wu, T., Lin, D., Liu, Y., Jaramillo, T.F., Nørskov, J.K., Cui, Y., 2018. High-efficiency oxygen reduction to hydrogen peroxide catalysed by oxidized carbon materials. Nat. Catal. 1, 156–162. https://doi.org/10.1038/s41929-017-0017-x.

Luo, T., Feng, H., Tang, L., Lu, Y., Tang, W., Chen, S., Yu, J., Xie, Q., Ouyang, X., Chen, Z., 2020. Efficient degradation of tetracycline by heterogeneous electro-Fenton process using Cu-doped Fe@Fe2O3: mechanism and degradation pathway. Chem. Eng. J. 382, 122970 https://doi.org/10.1016/j.cej.2019.122970.

Mailler, R., Gasperi, J., Coquet, Y., Buleté, A., Vulliet, E., Deshayes, S., Zedek, S., Mirande-Bret, C., Eudes, V., Bressy, A., Caupos, E., Moilleron, R., Chebbo, G., Rocher, V., 2016. Removal of a wide range of emerging pollutants from wastewater treatment plant discharges by micro-grain activated carbon in fluidized bed as tertiary treatment at large pilot scale. Sci. Total Environ. 542, 983–996. https://doi.org/10.1016/j.scitotenv.2015.10.153.

Maldonado-Hódar, F.J., Moreno-Castilla, C., Pérez-Cadenas, A.F., 2004. Surface morphology, metal dispersion, and pore texture of transition metal-doped monolithic carbon aerogels and steam-activated derivatives. Microporous Mesoporous Mater. 69, 119–125. https://doi.org/10.1016/j.micromeso.2004.02.001.

Maldonado-Hódar, F.J., Moreno-Castilla, C., Rivera-Utrilla, J., Hanzawa, Y., Yamada, Y., 2000. Catalytic graphitization of carbon aerogels by transition metals. Langmuir 16, 4367–4373. https://doi.org/10.1021/la991080r.

Matyszczak, G., Krzyczkowska, K., Fidler, A., 2020. A novel , two-electron catalysts for the electro-Fenton process. J. Water Process Eng. 36, 101242 https://doi.org/10.1016/j.jwpe.2020.101242.

Navalon, S., Dhakshinamoorthy, A., Alvaro, M., García, H., 2011. Heterogeneous Fenton catalysts based on activated carbon and related materials. ChemSusChem 4, 1712–1730. https://doi.org/10.1002/cssc.201100216.

Noe, J., Latus, A., Lagrost, C., Volanschi, E., Hapiot, P., 2012. Evidence for OH radical production during electrocatalysis of oxygen reduction on Pt surfaces: consequences and application. J. Am. Chem. Soc. 134, 2835–2841.
Oller, I., Plakas, K.V., Malato, S., 2021. Carbon-based cathodes degradation during electro-Fenton treatment at pilot scale : changes in H2O2 electrogeneration. Chemosphere 275, 129962. https://doi.org/10.1016/j.chemosphere.2021.129962.
Oturan, M.A., Aaron, J.-J., 2014. Advanced oxidation processes in water/wastewater treatment: principles and applications. A review. Crit. Rev. Environ. Sci. Technol. 44, 2577–2641. https://doi.org/10.1080/10643389.2013.829765.
Qin, N., Yu, S., Ji, Z., Wang, Y., Li, Y., Gu, S., Gan, Q., Wang, Z., Li, Z., Luo, G., Zhang, K., Lu, Z., 2022. Oxidation state as a descriptor in oxygen reduction electrocatalysis. CCS Chem 1–12. https://doi.org/10.31635/ccschem.022.202101531.
Qin, X., Zhao, K., Quan, X., Cao, P., Chen, S., Yu, H., 2021. Highly efficient metal-free electro-Fenton degradation of organic contaminants on a bifunctional catalyst. J. Hazard Mater. 416, 125859 https://doi.org/10.1016/j.jhazmat.2021.125859.
Qiu, T., Yang, J.G., Bai, X.J., Wang, Y.L., 2019. The preparation of synthetic graphite materials with hierarchical pores from lignite by one-step impregnation and their characterization as dye absorbents. RSC Adv. 9, 12737–12746. https://doi.org/10.1039/c9ra00343f.
Radhi, M.M., Jaffar Al-Mulla, E.A., Tan, W.T., 2014. Electrochemical characterization of the redox couple of Fe(III)/Fe(II) mediated by grafted polymer electrode. Res. Chem. Intermed. 40, 179–192. https://doi.org/10.1007/s11164-012-0954-6.
Ramos-Fernández, G., Canal-Rodríguez, M., Arenillas, A., Menéndez, J.A., Rodríguez-Pastor, I., Martin-Gullon, I., 2018. Determinant influence of the electrical conductivity versus surface area on the performance of graphene oxide-doped carbon xerogel supercapacitors. Carbon N. Y. 126, 456–463. https://doi.org/10.1016/j.carbon.2017.10.025.
Rosal, R., Rodríguez, A., Perdigón-Melón, J.A., Petre, A., García-Calvo, E., Gómez, M.J., Agüera, A., Fernández-Alba, A.R., 2010. Occurrence of emerging pollutants in urban wastewater and their removal through biological treatment followed by ozonation. Water Res. 44, 578–588. https://doi.org/10.1016/j.watres.2009.07.004.
Rufford, T.E., Hulicova-Jurcakova, D., Zhu, Z., Lu, G.Q., 2009. Empirical analysis of the contributions of mesopores and micropores to the double-layer capacitance of carbons. J. Phys. Chem. C 113, 19335–19343. https://doi.org/10.1021/jp905975q.
Sannino, D., 2020. Visible light active photocatalysts for the removal of organic emerging contaminants, visible light active structured photocatalysts for the removal of emerging contaminants. Elsevier. https://doi.org/10.1016/b978-0-12-818334-2.00005-5.
Schuepfer, D.B., Badaczewski, F., Guerra-castro, J.M., Hofmann, D.M., Heiliger, C., Smarsly, B., Klar, P.J., 2020. Assessing the structural properties of graphitic and non-graphitic carbons by Raman spectroscopy. Carbon N. Y. 161, 359–372. https://doi.org/10.1016/j.carbon.2019.12.094.
Siahrostami, S., Verdaguer-Casadevall, A., Karamad, M., Deiana, D., Malacrida, P., Wickman, B., Escudero-Escribano, M., Paoli, E.A., Frydendal, R., Hansen, T.W., Chorkendorff, I., Stephens, I.E.L., Rossmeisl, J., 2013. Enabling direct H2O2 production through rational electrocatalyst design. Nat. Mater. 12, 1137–1143. https://doi.org/10.1038/nmat3795.
Sing, K., 2001. The use of nitrogen adsorption for the characterisation of porous materials. Colloids Surfaces A Physicochem. Eng. Asp. 187– 188, 3–9. https://doi.org/10.1016/S0927-7757(01)00612-4.
Sun, X., Qi, H., Sun, Z., 2022. Bifunctional nickel foam composite cathode co-modified with CoFe@NC and CNTs for electrocatalytic degradation of atrazine over wide pH range. Chemosphere 286, 131972. https://doi.org/10.1016/j.chemosphere.2021.131972.
Takahagi, T., Ishitani, A., 1988. XPS study on the surface structure of carbon fibers using chemical modification and C1s line shape analysis. Carbon N. Y. 26, 389–395. https://doi.org/10.1016/0008-6223(88)90231-X.
Toh, R.J., Sofer, Z., Pumera, M., 2015. Transition metal oxides for the oxygen reduction reaction: influence of the oxidation states of the metal and its position on the periodic table. ChemPhysChem 16, 3527–3531. https://doi.org/10.1002/cphc.201500483.
Vallerot, J., Bourrat, X., Mouchon, A., Chollon, G., 2006. Quantitative structural and textural assessment of laminar pyrocarbons through Raman spectroscopy, electron diffraction and few other techniques. Carbon N. Y. 44, 1833–1844. https://doi.org/10.1016/j.carbon.2005.12.029.
Wang, Y., Alsmeyer, D.C., McCreery, R.L., 1990. Raman spectroscopy of carbon materials: structural basis of observed spectra. Chem. Mater. 2, 557–563. https://doi.org/10.1021/cm00011a018.
Wu, W.D., 2018. Active sites derived from heteroatom doping in carbon materials for oxygen reduction reaction. In: Ray, A., Mukhopadhyay, I., Pati, R.K. (Eds.), Electrocatalysts for Fuel Cells and Hydrogen Evolution - Theory to Design. IntechOpen, Rijeka. https://doi.org/10.5772/intechopen.77048. Ch. 3.
Xiao, F., Wang, Z., Fan, J., Majima, T., Zhao, H., Zhao, G., 2021. Selective electrocatalytic reduction of oxygen to hydroxyl radicals via 3-electron pathway with FeCo alloy encapsulated carbon aerogel for fast and complete removing pollutants. Angew. Chem. Int. Ed. 60, 10375–10383. https://doi.org/10.1002/anie.202101804.
Xu, P., Chen, W., Wang, Q., Zhu, T., Wu, M., Qiao, J., Chen, Z., Zhang, J., 2015. Effects of transition metal precursors (Co, Fe, Cu, Mn, or Ni) on pyrolyzed carbon supported metal-aminopyrine electrocatalysts for oxygen reduction reaction. RSC Adv. 5, 6195–6206. https://doi.org/10.1039/c4ra11643g.
Yadvinder-Singh, Kukal, S.S., Jat, M.L., Sidhu, H.S., 2014. Improving water productivity of wheat-based cropping systems in south asia for sustained productivity. Adv. Agron. 127, 157–258. https://doi.org/10.1016/B978-0-12-800131-8.00004-2.
Yang, W., Zhou, M., Oturan, N., Li, Y., Su, P., Oturan, M.A., 2019. Enhanced activation of hydrogen peroxide using nitrogen doped graphene for effective removal of herbicide 2,4-D from water by iron-free electrochemical advanced oxidation. Electrochim. Acta 297, 582–592. https://doi.org/10.1016/j.electacta.2018.11.196.
Zhai, D., Du, H., Li, B., Zhu, Y., Kang, F., 2011. Porous graphitic carbons prepared by combining chemical activation with catalytic graphitization. Carbon N. Y. 49, 725–729. https://doi.org/10.1016/j.carbon.2010.09.057.
Zhang, M., Dong, H., Zhao, L., Wang, D., Meng, D., 2019. A review on Fenton process for organic wastewater treatment based on optimization perspective. Sci. Total Environ. 670, 110–121. https://doi.org/10.1016/j.scitotenv.2019.03.180.
Zhao, H., Qian, L., Chen, Y., Wang, Q., Zhao, G., 2018. Selective catalytic two-electron O 2 reduction for onsite e ffi cient oxidation reaction in heterogeneous electro-Fenton process. Chem. Eng. J. 332, 486–498. https://doi.org/10.1016/j.cej.2017.09.093.